Materials Science & Engineering A 766 (2019) 138340

Contents lists available at ScienceDirect

Materials Science & Engineering A

journal homepage: www.elsevier.com/locate/msea

Improved trade-off between strength and plasticity in titanium based metastable beta type Ti-Zr-Fe-Sn alloys

C.D. Rabadia[a], Y.J. Liu[b], C.H. Zhao[c], J.C. Wang[a], S.F. Jawed[a], L.Q. Wang[d,**], L.Y. Chen[e], H. Sun[a], L.C. Zhang[a,*]

[a] School of Engineering, Edith Cowan University, 270 Joondalup Drive, Joondalup, Perth, WA, 6027, Australia
[b] School of Engineering, The University of Western Australia, 35 Stirling Highway, Perth, WA, 6009, Australia
[c] Guangxi Key Laboratory of Processing for Non-ferrous Metals and Featured Materials, Guangxi University, Nanning, 530004, China
[d] State Key Laboratory of Metal Matrix Composites, School of Material Science and Engineering, Shanghai Jiao Tong University, No. 800 Dongchuan Road, Shanghai, 200240, China
[e] School of Science, Jiangsu University of Science and Technology, Zhenjiang, Jiangsu, 212003, China

ARTICLE INFO

Keywords:
Titanium alloys
Laves phase
Mechanical properties
Deformation
Fracture mechanism
Dislocation density

ABSTRACT

An impressive strengthening ability of Laves phases is favorable to develop titanium alloys with an improved trade-off between strength and plasticity. Therefore, the Ti-xZr-7Fe-ySn (x = 25, 30, 35 wt% and y = 1, 2 wt%) alloys were first designed in such a manner that a Laves phase would precipitate in these alloys and then the investigated alloys were produced by cold crucible levitation melting. A hexagonal close-packed C14 type Laves phase along with a dominant fraction of body-centered cubic β phase are formed in all the as-cast Ti-xZr-7Fe-ySn alloys except in Ti-25Zr-7Fe-2Sn. The volume fraction of the Laves-C14 phase is found to be sensitive to the quantities of Zr and Sn. Amongst all the investigated alloys, Ti-35Zr-7Fe-2Sn shows a better dislocation-pinning ability in terms of dislocation density ($3.96 \times 10^{15}\,m^{-2}$), yield strength (1359 MPa) and hardness (437 HV), whereas Ti-25Zr-7Fe-1Sn shows a better deformation ability in terms of compressive strain at failure (36.2%) and plastic strain (31.9%). Crack propagation, regions of dimples and deformation bands are examined in the fracture analyses. Moreover, in this work, Ti-25Zr-7Fe-1Sn exhibits the best strength and plasticity trade-off in terms of a product of ultimate strength and compressive strain at failure (77.4 GPa %).

1. Introduction

Laves phases are intermetallic compounds which form in AB_2-type alloy compositions, where interestingly, more than 1400 different Laves phases (comprising different elements and melting points from 7 °C to more than 2000 °C) have been reported to date since the 1950s [1]. However, in the last decade, investigations on Laves phases as a reinforcement agent have greatly increased because Laves phases demonstrate superior strength, hardness, creep properties and very good corrosion and oxidation resistance [2]. Therefore, Laves phase alloys are suitable for many high-strength applications in aerospace, petrochemical, nuclear and automobile industries [3]. C14, C15 and C36 are the three most basic types of Laves phases and the prototype structures of C14, C15 and C36 types of Laves phases remain hexagonal close-packed (hcp) $MgZn_2$, face-centered cubic (fcc) $MgCu_2$ and dihexagonal $MgNi_2$ respectively [4,5]. Laves phases are usually considered as brittle phases [6–8]. However, recently many researches have demonstrated that Laves phase alloys exhibit improved toughness and plasticity when Laves phase precipitates in a body-centered cubic (bcc) matrix. This is because a bcc matrix comprises a greater number of slip systems and the more slip systems present in a matrix can improve bulk toughness and plasticity of Laves phase alloys [5,9,10].

As far as the bcc matrix is concerned, β type titanium (Ti) alloys are well-recognized to demonstrate a bcc matrix in microstructure with excellent mechanical properties such as high strength, hardness and plasticity along with superior corrosion, wear and fatigue properties [11–16]. Elements such as manganese (Mn), iron (Fe) and chromium (Cr) are inexpensive and strong β stabilizers which increase the stability of β phase even when small quantities of these elements are added to Ti alloys [17–19]. These inexpensive β stabilizers work as solute constituents to increase the yield strength ($\sigma_{0.2}$) and hardness (H) of Ti alloys [20,21]. Furthermore, although zirconium (Zr) and tin (Sn) are

* Corresponding author.
** Corresponding author.
E-mail addresses: wang_liqiang@sjtu.edu.cn (L.Q. Wang), lczhangimr@gmail.com, l.zhang@ecu.edu.au (L.C. Zhang).

https://doi.org/10.1016/j.msea.2019.138340
Received 22 July 2019; Received in revised form 25 August 2019; Accepted 26 August 2019
Available online 27 August 2019
0921-5093/

recognized as neutral elements, Zr and Sn can also improve the mechanical and corrosion properties when alloyed with Ti [22–25]. Additionally, Sn work as a β stabilizer even when only small quantities of Sn are added to Ti alloys [22,26].

The strength and plasticity trade-off is a well-known vital phenomenon for high-strength metallic materials [27–30]. In Laves phase alloys, the strength and plasticity trade-off can be achieved by appropriately tailoring the volume fraction of the Laves phase [7,9,10]. Nonetheless, firstly, the alloys should be designed such that the Laves phase forms in the microstructure and therefore, the quantities of alloying elements play a key role in the precipitation of Laves phase and in deciding the Strukturbericht designation (C14/C15/C36) of Laves phase [4]. The quantities of alloying elements can be selected considering the corresponding binary and ternary phase diagrams of the alloying elements. According to the Ti-Zr-Fe ternary phase diagram, the chances of the Laves phase formation remain higher if the quantities of Zr and Fe are added above 25 wt% and 5 wt% respectively to Ti alloys [31,32].

Considering the above points, the quaternary Ti-xZr-7Fe-ySn (x = 25, 30, 35 wt% and y = 1, 2 wt%) alloys were chosen in the present work with an aim to obtain an improved the trade-off between strength and plasticity. In the selected Ti-xZr-7Fe-ySn alloys, the quantities of Fe were kept at 7 wt%, while the quantities Zr and Sn were varied from 25 wt% to 35 wt% and from 1 wt% to 2 wt% respectively, in order to examine the effects of compositional quantities on the microstructure and mechanical properties of the Ti-xZr-7Fe-ySn alloys. According to the previous work on Ti-Zr-Sn alloys [33,34], the addition of small quantity of Sn (up to 2 wt% in this work) does not contribute to the Laves phase formation; therefore, it may enhance the β stability in the selected Ti-xZr-7Fe-ySn alloys [26]. In addition, for all the Ti-xZr-7Fe-ySn alloys, fractured-surface morphologies have been investigated to analyze crack propagation, dimple regions and slip bands. Furthermore, dislocation density after compression testing has been estimated using the XRD line profile analysis because dislocation density helps to determine the dislocation-pinning behavior of the investigated alloys. Moreover, a product of ultimate strength (σ_{max}) and compressive strain at failure (PUSCS) has been used to compare the strength and plasticity trade-off obtained for all the investigated alloys [35,36], because PUSCS is useful for alloys to be selected when σ_{max} and compressive deformation are considered for specific applications.

2. Materials and methods

The Ti-xZr-7Fe-ySn (x = 25, 30, 35 wt% and y = 1, 2 wt%) alloys were cast (in the form of ingot) under an argon atmosphere using alloying elements with 99.9% purity in a cold crucible levitation melting furnace. The cast ingots of the Ti-xZr-7Fe-ySn alloys were then rapidly quenched in a water-cooled copper crucible. The cylindrical rods from each cast ingot were produced from the core of the ingot with ~4.5 mm in diameter using wire electrical discharge machining and then, the cylindrical rods of the Ti-xZr-7Fe-ySn alloys were cut using a Buehler Isomet 1000. The abbreviated names in the form of TxSy for all the Ti-xZr-7Fe-ySn alloys were used, e.g., T25S1 was used to abbreviate Ti-25Zr-7Fe-1Sn, T35S2 was used to abbreviate Ti-35Zr-7Fe-2Sn and the similar abbreviation pattern was used to abbreviate the remaining Ti-xZr-7Fe-ySn alloys.

For all the investigated Ti-xZr-7Fe-ySn alloys, grinding and polishing operations were executed (as per the requirement of the specific analysis) according to standard metallographic procedures for preparing samples for phase and microstructure analyses as well as for mechanical testing. Scanning electron microscopy (SEM) was executed using a FEI Verios XHR 460 microscope to carry out the microstructure analyses. For all the investigated alloys, energy dispersive X-ray spectroscopy (EDX) was employed using an Oxford Instruments X-Max SDD detector (attached with a FEI Verios XHR 460 microscope) to obtain the compositional quantities and the EDX mapping images of alloying elements.

A PANalytical EMPYREAN X-ray diffractometer with a cobalt source (Co-Kα with a wavelength, λ of 0.1789 nm) was used to carry out the X-ray diffraction (XRD) tests in the present work. For all the investigated alloys, XRD tests were performed at a scan speed of 0.011°/s and at a step size of 0.003° between the 2θ angles of 30° and 110° for the phase characterization of the investigated alloys before and after compression testing. The XRD line profile analyses were carried out to estimate dislocation density of the β phase after compression testing using Eq. (1) which was derived based on the Williamson-Smallman method [37–39].

$$\rho_d = \frac{2\sqrt{3}\ \xi}{Db} \tag{1}$$

where ρ_d is dislocation density, ξ is lattice strain, D is crystallite size and b is burgers vector, $b = (a/2)\sqrt{h^2 + k^2 + l^2}$ for bcc and fcc crystal structures (where a is lattice parameter and h, k and l are miller indices) [40]. The lattice parameter of the β phase (a_β) was calculated for each alloy in the as-cast condition as well as after compression testing using a Nelson-Riley's extrapolation function: $(\cos^2\theta/\sin\theta) + (\cos^2\theta/\theta)$ [9,41,42]. The values of lattice strain and crystallite size were estimated using Eq. (2) suggested by Williamson and Hall [43–46] based on the broadening of XRD peaks.

$$B_{St}\cdot cos\theta = \frac{k\lambda}{D} + 2\xi\cdot sin\theta \tag{2}$$

where B_{St} is broadening of XRD peaks that has occurred due to lattice strain and crystallite size, θ is diffraction angle of a peak, k is constant (~1), D is crystallite size and ξ is lattice strain. The broadening of peaks can usually be measured in terms of a full-width half maximum, FWHM, which is a width of a peak (in radians) at the half of the maximum intensity of a peak. However, the total broadening of XRD peaks usually occurs due to crystallite size, lattice strain as well as due to the instrument used in a XRD test according to Eq. (3) [44,45].

$$B_O = B_{St} + B_I \tag{3}$$

where B_O is the observed/total broadening of peaks, B_{St} is the broadening of peaks that occurs due to lattice strain and crystallite size and B_I is the broadening of peaks that occurs due to the instrument used. This means that B_I should be subtracted from B_O in order to obtain the value of B_{St}. The value of B_I can be obtained from the observed peak broadening that occurs in a standard LaB_6 sample provided by the manufacturer of the diffractometer. The values of B_{St} in the present work were obtained directly from Highscore software provided by the manufacturer of the diffractometer, which gives the values of B_{St} after subtracting B_I. According to the Williamson-Hall plot [43–45], the values of $B_{St}\cdot cos\theta$ were plotted against the values of $2sin\theta$ for the peaks associated with the β phase. The crystallite size was then estimated using the value of y-intercept and the lattice strain was estimated from the slope of the Williamson-Hall plot [44,45]. The dislocation densities in the β phase for each alloy (after compression testing) were estimated considering the burgers vector, $b = (a/2) < 111 >$ [47].

As the features of microstructure correlate directly with the mechanical properties of a material [48–52], mechanical compression tests were performed according to ASTM E9 on at least 3 samples of each alloy using an Instron 5982 at a crosshead speed of 0.1 mm/min. Note that $\sigma_{0.2}$, σ_{max}, compressive strain at failure (ϵ_f) and plastic strain (ϵ_p) were calculated from the stress versus strain curves of the investigated alloys. All the aforementioned mechanical properties were reported with their corresponding average values. Compression tests were employed to determine the intrinsic deformation behavior of the alloys when the load in compression was applied to them, which is useful for high-strength materials especially used in compression-loading applications [53]. The values of true compressive stress and true compressive strain for the investigated alloys were calculated using Eqs. (4) and (5) respectively [54].

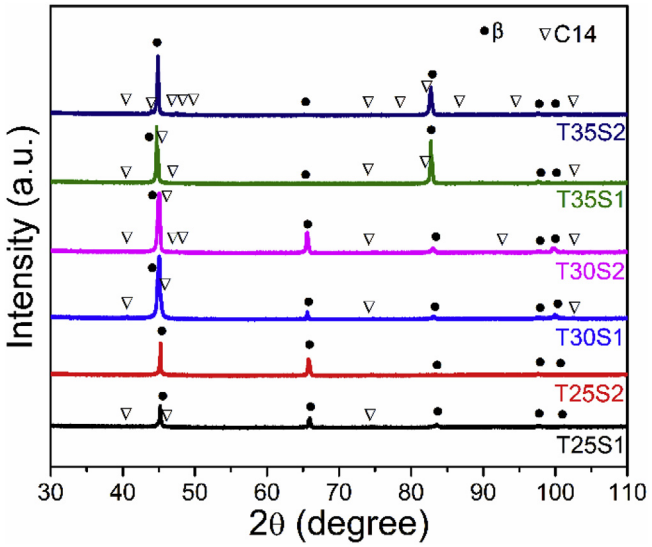

Fig. 1. The XRD profiles of the investigated Ti-xZr-7Fe-ySn alloys in the as-cast condition. Note that the abbreviation pattern in the forms of TxSy is used to label all the investigated Ti-xZr-7Fe-ySn alloys.

$$\varepsilon_{True} = -\ln(1 - e) \quad (4)$$

$$\sigma_{True} = \sigma_{Eng}.(1 - e) \quad (5)$$

where ε_{True} is true strain, e is engineering strain, σ_{True} is true stress, σ_{Eng} is engineering stress.

Moreover, at least 8 microhardness indents were taken using a Vickers indenter at an applied force of 5 kgf and a holding time of 20 s on a Zwick Roell ZHU. For fracture analyses, two types of samples for each alloy were prepared: (i) A sample was sectioned first from the centre after compression testing, followed by metallographic grinding and polishing operations to analyze the voids and crack propagation, (ii) A sample failed in compression testing was carefully cleaned and examined to analyze the dimple and cleavage regions as well as the deformation bands. Both types of fracture morphologies were examined by SEM using a FEI Verios XHR 460 microscope.

3. Results

3.1. Phase and microstructure analyses

Fig. 1 shows the XRD profiles obtained in the as-cast condition for all the investigated alloys. The XRD profile of T25S2 features the peaks of only a β phase with a bcc structure (Space group: *Im-3m*), whereas the XRD profiles of T25S1, T30S1, T30S2, T35S1 and T35S2 consist of the diffraction peaks of a β phase together with a C14 type Laves phase (Space group: $P6_3/mmc$) with an hcp structure. The diffraction angles of Laves phases usually follow the diffraction angles of their respective prototype structure. Hence, C14 phase is identified using an ICDD powder diffraction file of $MgZn_2$ (01-071-9623) [4,5,55] which is the prototype structure of C14 type phases. In Fig. 1, T35S2 shows the highest number of peaks related to the C14 phase, whereas all the investigated alloys show the same number of peaks related to the β phase. This means that T35S2 should comprise the highest volume fraction of C14 phase ($V_{f,\ C14}$) amongst all the investigated alloys. Furthermore, the diffraction angles shift slightly toward the low-angle side as the quantities of Zr and Sn increase in the investigated alloys and therefore, the lattice parameter of β phase (a_β) in the as-cast condition decreases as presented in Table 1. The obtained-values of a_β for T25S1, T25S2 and T30S1 are lower than the typical a_β of Ti (0.3306 nm), whereas the obtained values of a_β for T30S2, T35S1 and T35S2 are greater than the typical a_β of Ti (0.3306 nm). This also reveals that the a_β increases as the quantities of Zr and Sn increase in the investigated alloys [56].

Fig. 2 illustrates the microstructural features of the as-cast Ti-xZr-7Fe-ySn alloys. The microstructure images of T25S1, T30S1, T30S2, T35S1 and T35S2 clearly depict the segregated-eutectic morphologies of the Laves phase (white) and the near-equiaxed morphologies of the β phase (dark grey) (Fig. 2). The XRD analyses confirm that the type of Laves phase (segregated in the T25S1, T30S1, T30S2, T35S1 and T35S2 alloys) is C14 type. The β-grain boundary in T25S2 can also be seen in the inset image of Fig. 2b. In addition, other than the morphologies of β and Laves phases, bright-faded morphologies are observed in the back-scattered SEM images shown in Fig. 2. The bright-faded morphologies visible in the back-scattered SEM images (Fig. 2) should be the concentration of an element having a greater atomic number because an element with a greater atomic number produces a relatively higher elastic collision with electrons than an element with a lower atomic number when a detector of back-scattered electron is used [57]. Consequently, in a back-scattered SEM image, the regions of an element having a relatively greater atomic number look brighter than the regions of an element having a relatively lower atomic number [57,58]. The further discussion on the bright-faded morphologies will be covered later in the following sections.

From the SEM images, the values of $V_{f,\ C14}$ were estimated using ImageJ software for the Ti-xZr-7Fe-ySn alloys comprising the eutectic-Laves phase morphologies. Table 1 presents the values of $V_{f,\ C14}$ for the alloys comprising Laves phase (i.e., T25S1, T30S1, T30S2, T35S1 and T35S2). In the microstructure of the T25S1 alloy (Fig. 2a), the Laves phase morphologies with $V_{f,\ C14}$ of only 0.1 ± 0.04% are found over the grain boundary (Fig. 2a inset) and subsequently, as the quantities of Zr and Sn increase, the values of $V_{f,\ C14}$ increase in the T30S1, T30S2, T35S1 and T35S2 alloys (Table 1).

Quantitative point analyses using an EDX detector were carried out over the multiple regions of eutectic-Laves phase morphologies, β phase and bright-faded morphologies. In Fig. 2, the points 1, 4, 6, 9, 12 and 15 are marked over the β phase and the points 3, 5, 8, 11, 14 and 17 are marked over the bright-faded morphologies in the T25S1, T25S2, T30S1, T30S2, T35S1 and T35S2 alloys respectively, whereas the points 2, 7, 10, 13 and 16 are marked over the eutectic-Laves phase morphologies in the T25S1, T30S1, T30S2, T35S1 and T35S2 alloys respectively. The average quantities of each alloying element over the marked ("x") regions/phases in Fig. 2 are obtained from EDX, which are presented for each alloy in Table 2. For all the investigated alloys, the quantities of alloying elements measured over the β phase (points 1, 4, 6, 9, 12 and 15) are almost same as their corresponding nominal quantities (Table 2). In the quantities of alloying elements measured over the eutectic-Laves phase morphologies (points 2, 7, 10, 13 and 16), the quantities of Fe are greater than the twofold values of their corresponding nominal quantities. Further, the quantities of Zr are greater than their corresponding nominal quantities, whereas the quantities of Ti and Sn are less than their corresponding nominal quantities, in the T25S1, T30S1, T30S2, T35S1 and T35S2 alloys (Table 2). This demonstrates that the Laves (C14 type) phase in the present work is composed of Fe and Zr. Moreover, the quantities of Zr measured over the bright-faded morphologies (points 3, 5, 8, 11, 14 and 17) are greater than their corresponding nominal quantities and less than the quantities of Zr found over the Laves phase morphologies (points 2, 7, 10, 13 and 16), whereas the quantities of Ti, Fe and Sn over the bright-faded morphologies are almost same or less than their corresponding nominal quantities (Table 2).

EDX mapping for all the investigated Ti-xZr-7Fe-ySn alloys were performed. Fig. 3 depicts the EDX mapping images obtained for T30S2, as an example, from the corresponding back-scattered SEM image. Note that identical EDX mapping results (related to the Laves phase and bright-faded morphologies) are found for the rest of the investigated alloys. In Fig. 3, the eutectic morphologies of Laves (C14) phase (white) and the β phase (dark grey) are shown in the back-scattered SEM image. The EDX mapping images shown in Fig. 3 also confirm that Laves (C14)

Table 1
Lattice parameter of β phase in the as-cast condition (a_β*) and after compression testing (a_β**) along with the microstructural features (in the as-cast condition) such as the values of volume fraction of β phase ($V_{f,\ \beta}$) and C14 phase ($V_{f,\ C14}$), lamellar spacing, length and width of Laves phase (C14) morphologies for all the Ti-xZr-7Fe-ySn alloys.

Alloys	Chemical compositions (wt%)	a_β* (nm)	a_β** (nm)	$V_{f,\ \beta}$ (%)	$V_{f,\ C14}$ (%)	Lamellar spacing (nm)	Length of Laves phase (μm)	Width of Laves phase (μm)
T25S1	Ti-25Zr-7Fe-1Sn	0.3275	0.3290	99.9 ± 0.04	0.1 ± 0.04	183 ± 67	21 ± 16	5 ± 5
T25S2	Ti-25Zr-7Fe-2Sn	0.3283	0.3296	100.0 ± 0.00	–	–	–	–
T30S1	Ti-30Zr-7Fe-1Sn	0.3305	0.3312	99.5 ± 0.06	0.5 ± 0.06	348 ± 155	42 ± 30	7 ± 4
T30S2	Ti-30Zr-7Fe-2Sn	0.3309	0.3314	98.4 ± 0.40	1.6 ± 0.40	464 ± 171	38 ± 28	8 ± 5
T35S1	Ti-35Zr-7Fe-1Sn	0.3320	0.3324	95.7 ± 0.17	4.3 ± 0.17	676 ± 305	101 ± 51	13 ± 11
T35S2	Ti-35Zr-7Fe-2Sn	0.3326	0.3329	91.7 ± 0.10	8.3 ± 0.10	798 ± 324	206 ± 88	20 ± 16

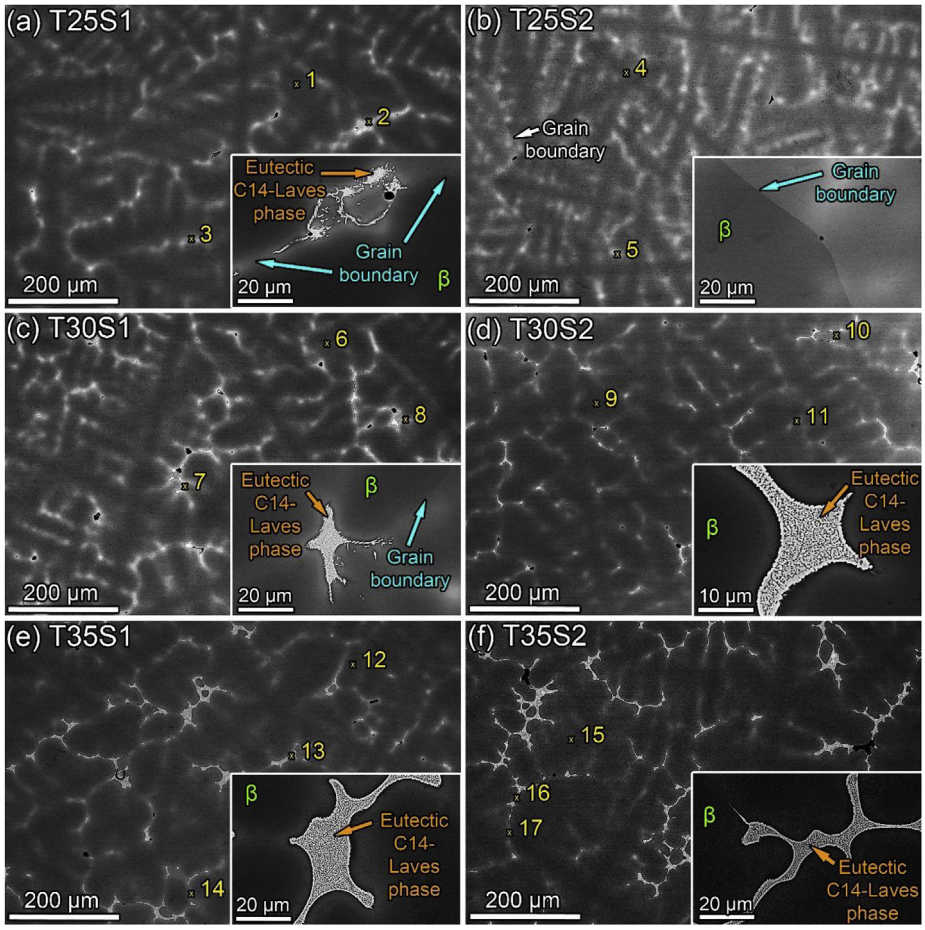

Fig. 2. The back-scattered SEM images of the as-cast Ti-xZr-7Fe-ySn alloys. The inset images in (a) to (f) are the corresponding high-magnification images of (a)–(f). Note that the abbreviation pattern in the forms of TxSy is used to present names of all the investigated alloys.

phase in T30S2 is composed of Fe and Zr as the clear segregations of Fe and Zr are found in the corresponding EDX mapping images of Fe and Zr. By contrast, Ti is greatly located at the regions of the β phase and excluded from the regions of Laves phase. Furthermore, Sn is concentrated slightly over the Laves phase and uniformly concentrated over the β phase. It is interesting to note that the concentration of only Zr is found over the bright-faded morphologies, where the other three elements (i.e., Ti, Fe and Sn) are concentrated in the same way as they concentrated over the regions of β phase. This indicates that the bright-faded morphologies present in the microstructures of all the investigated Ti-xZr-7Fe-ySn alloys are mainly composed of Zr [10]. In this work, the EDX mapping results shown in Fig. 3 are in good agreement with the EDX results shown in Table 2. In addition, it is important to note that the fraction of bright-faded morphologies in T30S2 and T35S2 are less than those found in T30S1 and T35S1 respectively (Fig. 2). This indicates that the bright-faded regions evolve into a Laves phase if the required quantities of alloying elements are added to alloys. Therefore, the values of $V_{f,\ C14}$ of T30S2 and T35S2 are greater than those of T30S1 and T35S1 respectively.

3.2. Mechanical properties

Fig. 4 presents the engineering and true stress versus strain curves obtained in compression testing for all the investigated alloys. True stress versus strain curves of a polycrystalline material in tension and in compression remain almost identical [59]. As a result, the behavior of a polycrystalline material in tension can be predicted based on its true compressive stress versus strain curve [59]. Therefore, true stress versus strain curves of the investigated alloys are presented in the present work (Fig. 4b). The engineering and true stress versus strain curves shown in Fig. 4 reveal that all the Ti-xZr-7Fe-ySn alloys exhibit some yielding and some level of plastic deformation before failure.

Table 2
Designed chemical compositions and the quantities of alloying elements measured (over the points marked in Fig. 2) in the EDX point analyses for all the investigated alloys.

Alloys	Chemical compositions (wt%)	Points marked in Fig. 2	The quantities of alloying elements			
			Ti (wt%)	Zr (wt%)	Fe (wt%)	Sn (wt%)
T25S1	Ti-25Zr-7Fe-1Sn	1	68.2 ± 0.5	23.4 ± 0.8	7.2 ± 0.5	1.2 ± 0.2
		2	34.6 ± 0.4	42.1 ± 0.6	22.8 ± 0.3	0.5 ± 0.3
		3	59.8 ± 1.4	31.9 ± 1.9	7.6 ± 0.6	0.7 ± 0.1
T25S2	Ti-25Zr-7Fe-2Sn	4	67.7 ± 0.4	23.2 ± 0.3	7.0 ± 0.1	2.1 ± 0.1
		5	62.8 ± 1.0	28.3 ± 1.1	7.4 ± 0.3	1.5 ± 0.1
T30S1	Ti-30Zr-7Fe-1Sn	6	61.9 ± 1.7	29.5 ± 1.6	7.3 ± 1.0	1.3 ± 0.1
		7	37.7 ± 1.8	44.5 ± 0.7	17.4 ± 1.1	0.4 ± 0.1
		8	52.7 ± 2.3	40.0 ± 3.0	6.6 ± 0.7	0.7 ± 0.1
T30S2	Ti-30Zr-7Fe-2Sn	9	61.4 ± 1.8	29.2 ± 0.9	7.1 ± 1.1	2.3 ± 0.2
		10	36.1 ± 1.1	41.1 ± 0.7	22.1 ± 1.5	0.7 ± 0.1
		11	56.7 ± 0.2	34.5 ± 0.3	7.4 ± 0.2	1.4 ± 0.1
T35S1	Ti-35Zr-7Fe-1Sn	12	57.1 ± 3.6	35.1 ± 3.7	6.8 ± 0.4	1.0 ± 0.4
		13	38.3 ± 1.7	41.0 ± 0.4	20.4 ± 1.8	0.3 ± 0.1
		14	55.0 ± 0.6	37.1 ± 0.8	7.1 ± 0.1	0.8 ± 0.1
T35S2	Ti-35Zr-7Fe-2Sn	15	57.2 ± 1.3	33.8 ± 1.3	7.1 ± 0.2	1.9 ± 0.2
		16	37.3 ± 3.6	39.0 ± 1.3	23.1 ± 2.7	0.6 ± 0.3
		17	56.4 ± 1.2	35.3 ± 1.2	6.8 ± 0.1	1.5 ± 0.1

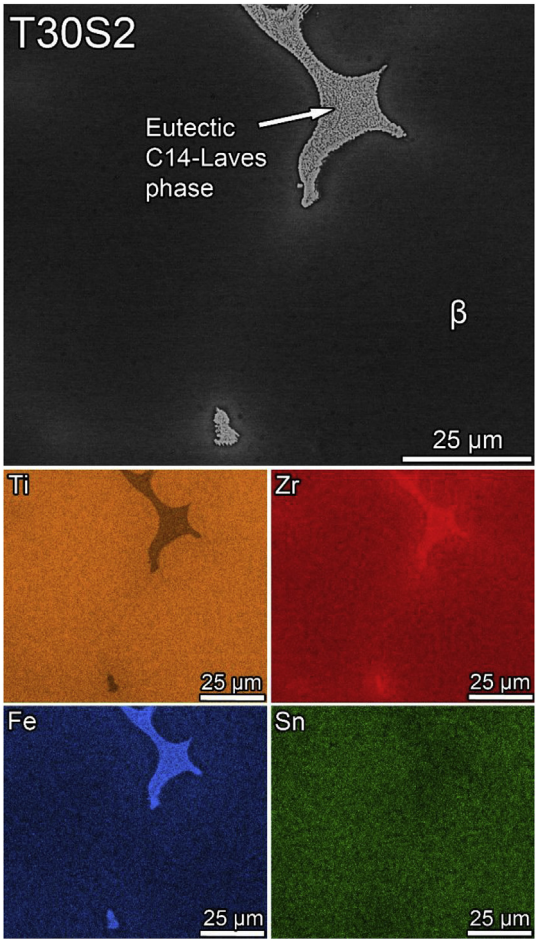

Fig. 3. The EDX mapping images obtained for T30S2 (Ti-30Zr-7Fe-2Sn) from the corresponding back-scattered SEM image. Identical EDX mapping results (related to the Laves phase and bright-faded morphologies) are found for the rest of the investigated alloys.

Table 3 and Table 4 present the mechanical properties which are obtained from the engineering and true stress versus strain curves respectively for the investigated alloys. In general, as deformation continues in the plastic zone of a material during compression testing, the instantaneous cross-sectional area of a sample increases and as a result, true strain remains higher than engineering strain, whereas true stress remains lower than engineering stress [56,59]. The similar effects can be seen for the true stress and true strain values (including true ϵ_f and true ϵ_p) of the investigated alloys (Fig. 4, Tables 3 and 4). Note that from now onwards, only engineering mechanical properties of the investigated alloys have been used in the succeeding discussion.

Fig. 5 correlates the values of engineering $\sigma_{0.2}$ and H for all the Ti-xZr-7Fe-ySn alloys. It can be seen from Figs. 4a and 5 that all the Ti-xZr-7Fe-ySn alloys demonstrate $\sigma_{0.2}$ and H exceeding 1.2 GPa and 375 HV respectively because of comprising 7 wt% of Fe in their corresponding alloy compositions. This indicates that such high $\sigma_{0.2}$ and H in the investigated Ti-xZr-7Fe-ySn alloys are attributed to solid-solution strengthening produced by the quantity of Fe (7 wt% in all the as-cast alloys) because Fe acts as a solute constituent and can produce solid-solution strengthening due to having a lower atomic radius (0.1260 nm) than Ti (0.1470 nm). On the other hand, the values of $\sigma_{0.2}$ and H increase with an identical trend as the quantities of Zr and Sn increase in the as-cast alloys (Fig. 5). This demonstrates that the further increase in $\sigma_{0.2}$ (above ~ 1.2 GPa) and H (above ~ 375 HV) in the investigated alloys occurs due to precipitation strengthening [60] produced by $V_{f,\ C14}$ and/or by the bright-faded morphologies. Consequently, T35S2 exhibits the highest values of $\sigma_{0.2}$ (1359 ± 28 MPa) and H (437 ± 23 HV), whereas T25S1 exhibits the lowest values of $\sigma_{0.2}$ (1207 ± 10 MPa) and H (377 ± 14 HV) amongst the as-cast Ti-xZr-7Fe-ySn alloys. Based on the results presented in Fig. 5, it can be deduced that the maximum dislocation-pinning should have occurred in T35S2, whereas the minimum dislocation-pinning should have occurred in T25S1 amongst all the as-cast alloys. In addition, Table 3 reveals that the (engineering) values of σ_{max}, ϵ_f and ϵ_p correlate to one another and decrease as the quantities of Zr and Sn increase in the Ti-xZr-7Fe-ySn alloys. As a consequence, amongst all the Ti-xZr-7Fe-ySn alloys, T25S1 displays the highest values of σ_{max} (2140 ± 53 MPa), ϵ_f (36.2 ± 0.5%) and ϵ_p (31.9 ± 0.7%), whereas T35S2 displays the lowest values of σ_{max} (1595 ± 45 MPa), ϵ_f (17.5 ± 1.3%) and ϵ_p (12.5 ± 1.1%).

3.3. Fracture behavior

Fig. 6 shows the metallographically-prepared fractured surface morphologies captured in a back-scattered electron mode for the Ti-xZr-7Fe-ySn alloys to analyze the crack propagation in the investigated alloys. The bright-faded morphologies are shown as Zr segregation in Fig. 6 because the bright-faded morphologies are mainly composed

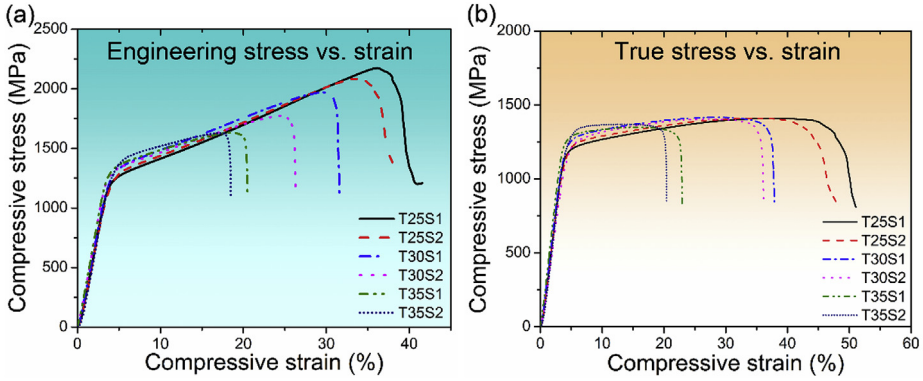

Fig. 4. (a) Engineering stress versus (vs.). strain and (b) True stress versus (vs.) strain curves obtained in compression testing for all the investigated alloys. Note that the abbreviation pattern in the forms of TxSy is used to present names of all the investigated alloys.

Table 3
The engineering mechanical properties such as ultimate compressive strength ($\sigma_{max,\ E}$), compressive strain at failure ($\epsilon_{f,\ E}$) and plastic strain ($\epsilon_{p,\ E}$) along with dislocation density (ρ_d) and a product of σ_{max} and ϵ_f (PUSCS) for the Ti-xZr-7Fe-ySn alloys.

Alloys	Chemical compositions (wt%)	$\sigma_{max,\ E}$ (MPa)	$\epsilon_{f,\ E}$ (%)	$\epsilon_{p,\ E}$ (%)	$\rho_d \times 10^{15}(m^{-2})$	PUSCS (GPa %)
T25S1	Ti-25Zr-7Fe-1Sn	2140 ± 53	36.2 ± 0.5	31.9 ± 0.7	0.21	77.4
T25S2	Ti-25Zr-7Fe-2Sn	2084 ± 52	33.6 ± 0.6	28.6 ± 0.6	0.24	70.0
T30S1	Ti-30Zr-7Fe-1Sn	2002 ± 43	29.7 ± 2.0	25.6 ± 2.0	2.58	59.5
T30S2	Ti-30Zr-7Fe-2Sn	1851 ± 48	25.6 ± 2.4	20.4 ± 2.6	2.77	47.4
T35S1	Ti-35Zr-7Fe-1Sn	1676 ± 57	19.0 ± 1.9	14.7 ± 2.0	3.22	31.8
T35S2	Ti-35Zr-7Fe-2Sn	1595 ± 45	17.5 ± 1.3	12.5 ± 1.1	3.96	27.9

Table 4
The true mechanical properties such as yield strength ($\sigma_{0.2,\ T}$), compressive strain at failure ($\epsilon_{f,\ T}$) and plastic strain ($\epsilon_{p,\ T}$) of the investigated alloys.

Alloys	Chemical compositions (wt%)	$\sigma_{0.2,\ T}$ (MPa)	$\epsilon_{f,\ T}$ (%)	$\epsilon_{p,\ T}$ (%)
T25S1	Ti-25Zr-7Fe-1Sn	1182 ± 24	44.5 ± 1.0	39.4 ± 1.6
T25S2	Ti-25Zr-7Fe-2Sn	1194 ± 16	39.7 ± 0.6	34.5 ± 0.9
T30S1	Ti-30Zr-7Fe-1Sn	1208 ± 18	36.4 ± 2.1	32.1 ± 2.0
T30S2	Ti-30Zr-7Fe-2Sn	1228 ± 21	31.6 ± 2.8	26.0 ± 2.5
T35S1	Ti-35Zr-7Fe-1Sn	1253 ± 19	23.5 ± 1.8	19.2 ± 1.7
T35S2	Ti-35Zr-7Fe-2Sn	1276 ± 40	21.2 ± 1.6	16.2 ± 1.8

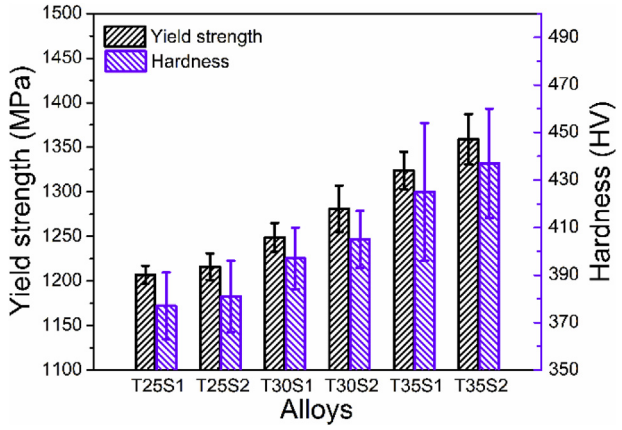

Fig. 5. Engineering yield strength ($\sigma_{0.2}$) and hardness (H) of the Ti-xZr-7Fe-ySn alloys. Note that the abbreviation pattern in the forms of TxSy is used to present names of all the investigated alloys.

with Zr. It has been acknowledged in the literature that nucleation followed by coalescence of voids occurs before the formation of crack [61]. Voids and coalescence of voids can be seen along the bright-faded morphologies (Zr segregation) at many places, which are shown using a series of yellow arrows in Fig. 6a and b for T25S1 and T25S2 respectively. This indicates that fractures in T25S1 and T25S2 occur along the Zr segregations. Further, the cracks propagate along the eutectic morphologies of Laves-C14 phase in Fig. 6c–f captured for T30S1, T30S2, T35S1 and T35S2 respectively. In addition, the deformation induced slip bands also form in all the Ti-xZr-7Fe-ySn alloys. The slip bands in Fig. 6 are shown using multiple series of green arrows.

Figs. 7 and 8 illustrate the fractured-surface morphologies of the Ti-xZr-7Fe-ySn alloys. Dimples usually form over a fractured surface that possesses a high deformability [62]. As discussed above, the deformability of a bcc phase remains higher than an hcp phase and consequently, bcc grains display dimples over the fractured surface [63]. In the present work, dimples are found over the fractured surfaces of the Ti-xZr-7Fe-ySn alloys; nonetheless, the cleavage facets increase as the plastic deformation in terms of ϵ_p decreases in the investigated alloys (Figs. 7e, 8a and 8c and 8e). Hence, the investigated alloys with 25 wt% of Zr show many regions of dimples and subsequently, the regions of dimples decrease in the investigated alloys with 30 wt% of Zr, followed by the investigated alloys with 35 wt% of Zr. Furthermore, fine dimples can be seen on fractured surfaces of the Ti-xZr-7Fe-ySn alloys including T35S1 (Fig. 8d) and T35S2 (Fig. 8f) which demonstrate less values of ϵ_p compared to the rest of the investigated alloys. This suggests that dimple morphologies in all the investigated alloys should have formed over the regions of the β phase which is known to display fine dimples even at low ϵ_p values [38].

The features of cracks can also be seen in the fractured surfaces of T30S1, T30S2, T35S1 and T35S2 (Figs. 7 and 8). The features of the cracks found in Fig. 8a, 8c and 8e reveal intergranular fracture in the T30S2, T35S1 and T35S2 alloys respectively. Moreover, slip bands are also found in the fractured surface morphologies of the Ti-xZr-7Fe-ySn alloys. The deformation induced slip activities should also have occurred in the regions of the β phase in all the Ti-xZr-7Fe-ySn alloys. Multiple wavy slip bands are shown in Fig. 7d inset for T25S2. Fig. 7d inset reveals that slip bands are not able to cross the grain boundary and therefore, slip bands are accumulated near the grain boundary because grain boundaries possess defects in the atomic sequence as discussed above [12]. In addition, these multiple wavy slip bands form in the

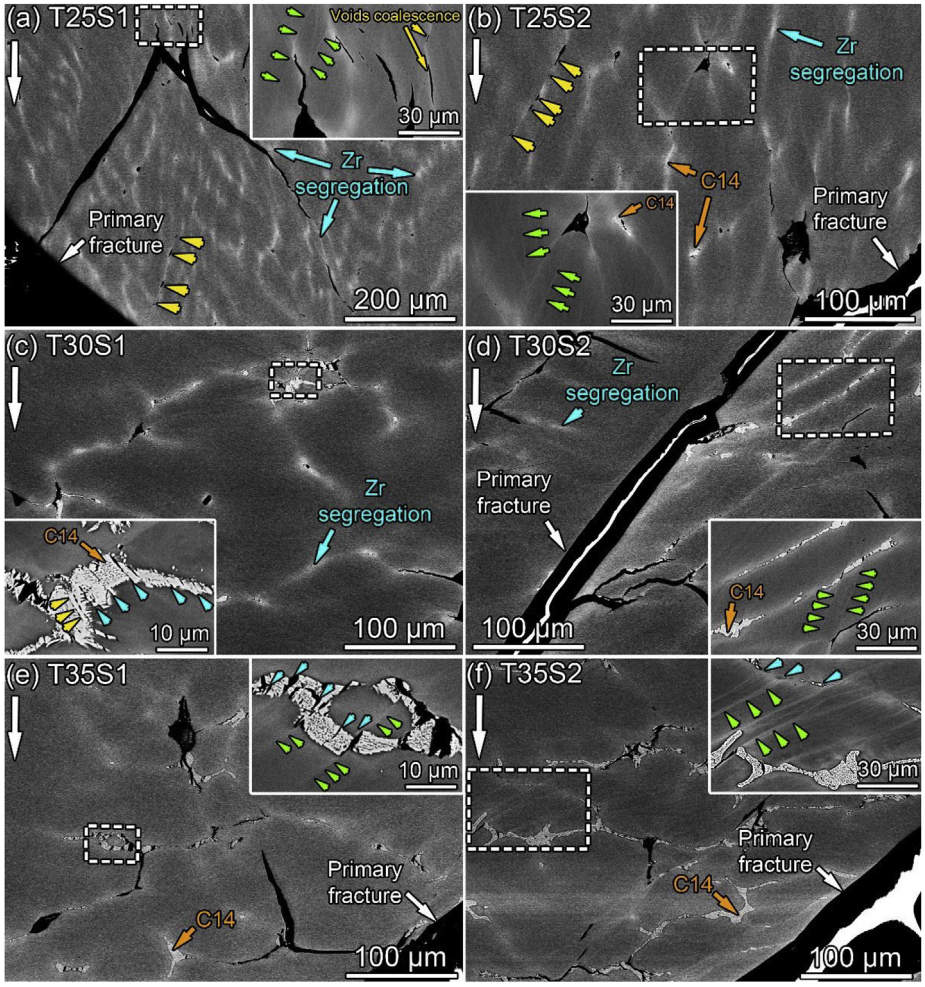

Fig. 6. The back-scattered SEM images of the fractured surfaces (prepared metallographically) for all the Ti-xZr-7Fe-ySn alloys. The insets shown in (a) to (f) are captured at high-magnification over the regions indicated by white-dashed rectangles in (a) to (f) respectively. The big-white (downward) arrows indicate the compression direction. Note that the abbreviation pattern in the forms of TxSy is used to present names of all the investigated alloys.

different slip planes as well as in the different slip directions depending on the number of active slip systems and the texture of the grains G1 and G2 shown in Fig. 7d inset [64]. The number of slip bands in grains G1 and G2 are different because different slip systems possess a different value of Peierls stress [63].

4. Discussion

4.1. Microstructure and mechanical properties

According to the literature, the occurrence of Laves phase segregation mostly depends on the size misfit that occurs between atoms in an alloy [65]. Therefore, a Laves phase composed of Zr and Fe usually forms in the alloying systems comprising the required quantities of Zr and Fe because there is a significant difference in atomic radii of Zr (0.1600 nm) and Fe (0.1280 nm). Laves phases composed of Zr and Fe have been reported in much literature [5,32,66]. The grain boundaries comprise crystal defects and usually increase Gibbs excess-free energy in an alloy without a solute constituent [65]. Therefore, alloys without solute particles usually show coarse grains in the microstructure. However, the interaction of solute atoms with an elastic strain field around grain boundaries decrease the Gibbs excess-free energy of a system and as a consequence, grain boundaries become the preferred regions for the Laves phase segregation [65]. Therefore, in the present work, the Laves phase in the T25S1, T30S1, T30S2, T35S1 and T35S2 alloys is mostly precipitated on the grain boundaries (Fig. 2).

The values of $V_{f,\ C14}$ increase as the quantities of Sn increase from 1 wt% in T30S1 and T35S1 to 2 wt% in T30S2 and T35S2. The similar kind of trend is not noted when the quantity of Sn increases from 1 wt% in T25S1 to 2 wt% in T25S2 despite the fact that T25S1 comprises the eutectic-Laves phase morphologies in the microstructure. This possibly occurs due to the high β stability of T25S2 as compared to T25S1 because the quantity of Sn improves the β stability when added in Ti alloys [26]. Nonetheless, in T30S2 and T35S2, the β stability achieved due to the addition of 2 wt% Sn cannot restrict the precipitation of Laves phase resulted from higher quantities of Zr (i.e., 30 wt% and 35 wt%) in T30S2 and T35S2. This demonstrates that the quantity of Zr plays an important role in the Laves phase precipitation in the Ti-xZr-7Fe-ySn alloys, which can also be confirmed based on the phase diagram of the Ti-Zr-Fe system [31,32].

Previous findings have reported that Laves phase precipitates subsequently in the form of particle-like, rod-like and eutectic morphologies as the volume fraction of Laves phase increases [9,10,67]. Moreover, the size (including length and width) of eutectic morphologies along with lamellar spacing inside the eutectic morphologies also increase as the volume fraction of the Laves phase increases [10]. Hence, in the present work, the approximate length and width of Laves phase morphologies along with lamellar spacing inside the eutectic morphologies were measured using ImageJ software for the investigated Ti-xZr-7Fe-ySn alloys comprising eutectic-Laves phase morphologies (i.e., T25S1, T30S1, T30S2, T35S1 and T35S2) and the corresponding results are summarized in Table 1. Note that the multiple

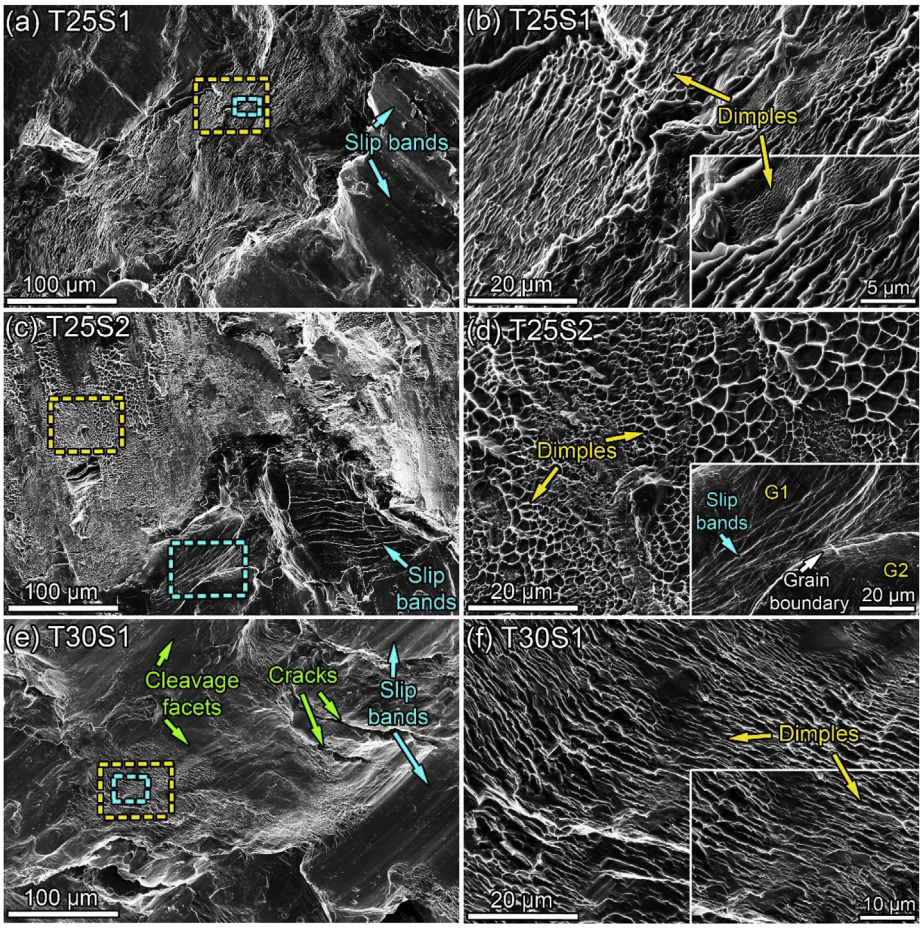

Fig. 7. The fractured morphologies of (a) T25S1, (c) T25S2 and (e) T30S1. (b), (d) and (f) are the high-magnification images of the regions shown using yellow-dashed rectangles in (a), (c) and (e) respectively. The inset images in (b), (d) and (f) are the high-magnification images of the regions shown using skyblue-dashed rectangles in (a), (c) and (e) respectively. Note that the abbreviation pattern in the forms of TxSy is used to present names of the investigated alloys. (For interpretation of the references to colour in this figure legend, the reader is referred to the Web version of this article.)

measurements for the length of Laves phase were taken along the direction in which the Laves phase is precipitated, while the multiple measurements for the width of the Laves phase were taken across the direction in which Laves phase is precipitated. Lamellar spacing, length and width of the Laves phase (C14) were measured because these parameters directly influence the mechanical properties [10,20]. Table 1 shows that the values of lamellar spacing, length and width of the Laves phase (C14) increase as the quantities of Zr and Sn increase in the T25S1, T30S1, T30S2, T35S1 and T35S2 alloys. T25S1 demonstrates the lowest values of lamellar spacing (183 ± 67 nm), length (21 ± 16 μm) and width (5 ± 5 μm) of the Laves phase (C14), whereas T35S2 demonstrates the highest values of lamellar spacing (798 ± 324 nm), length (206 ± 88 μm) and width (20 ± 16 μm) of the Laves phase (C14). This indicates that the values of lamellar spacing as well as length and width of the Laves phase increase as $V_{f,\ C14}$ increases in the T25S1, T30S1, T30S2, T35S1 and T35S2 alloys. As a result, the values of σ_{max}, ϵ_f and ϵ_p are also influenced by and related inversely with the values of lamellar spacing (inside the eutectic-Laves phase morphologies), length and width of the Laves phase morphologies (Table 1) in T25S1, T30S1, T30S2, T35S1 and T35S2.

It is worth noting that despite possessing Laves phase morphologies in the microstructure, T25S1 demonstrates the greater values of σ_{max}, ϵ_f and ϵ_p than those of the values obtained for T25S2 (Table 3) because T25S2 comprises a high fraction of bright-faded morphologies in the microstructure as compared to T25S1 (Fig. 2). These bright-faded regions in T25S2 are essentially composed of a higher quantity of Zr (28.3 ± 1.1 wt%) than the quantity of Zr present (23.2 ± 0.3 wt%) in the β matrix of T25S2. Further, Zr has a greater atomic radius (0.1600 nm) than Ti (0.1470 nm) and therefore, due to the size misfit effect, the arms of bright-faded morphologies act as barriers to the motion of dislocations and eventually become the high-stress concentrated regions due to dislocation pinning. Therefore, T25S2 fails earlier than T25S1 in compression testing and shows the lower values of σ_{max} (2084 ± 52 MPa), ϵ_f (33.6 ± 0.6%) and ϵ_p (28.6 ± 0.6%) and the higher values of $\sigma_{0.2}$ (1216 ± 15 MPa) and H (381 ± 15 HV) than those of T25S1.

Fig. 9 depicts the XRD profiles obtained after compression testing for the Ti-xZr-7Fe-ySn alloys. The number of peaks related to C14 phase in the XRD profiles obtained after compression testing (Fig. 9) are less than those obtained in the as-cast condition (Fig. 1). This happens because the β grains and Laves phase morphologies are compressed during compression testing and consequently, the area fractions of the β grains and Laves phase morphologies remain less (due to the refinement of grains) in a sample prepared for an XRD test after compression testing as compared to a sample prepared for an XRD test in the as-cast condition. On the other hand, cracks are propagated along the brittle-Laves phase [9,10], as a result, the regions of Laves phase are covered by the regions of cracks. Therefore, the area fraction of Laves phase remains less after compression testing (performed until failure of an alloy). Therefore, the XRD may not be able to detect all the peaks related to C14 phase which were present before compression testing [68]. The values of a_β after compression testing were calculated and the corresponding results are summarized in Table 1 to compare the values of a_β in the as-cast condition and after compression testing. Distortion of lattice and grain-refinement occur when a material undergoes a rolling operation or a compression testing [38,69] and hence, the values of a_β after compression testing increase for all the Ti-xZr-7Fe-ySn alloys. It can also be noted that a peak related to C14 phase (at around 40°) is found in the XRD profile of T25S2 (Fig. 9) after compression testing, which was not evident in the as-cast condition (Fig. 1). This indicates that the transformation of the Laves-C14 phase (with the little amount) occurs in T25S2 after compression testing from the β phase. A

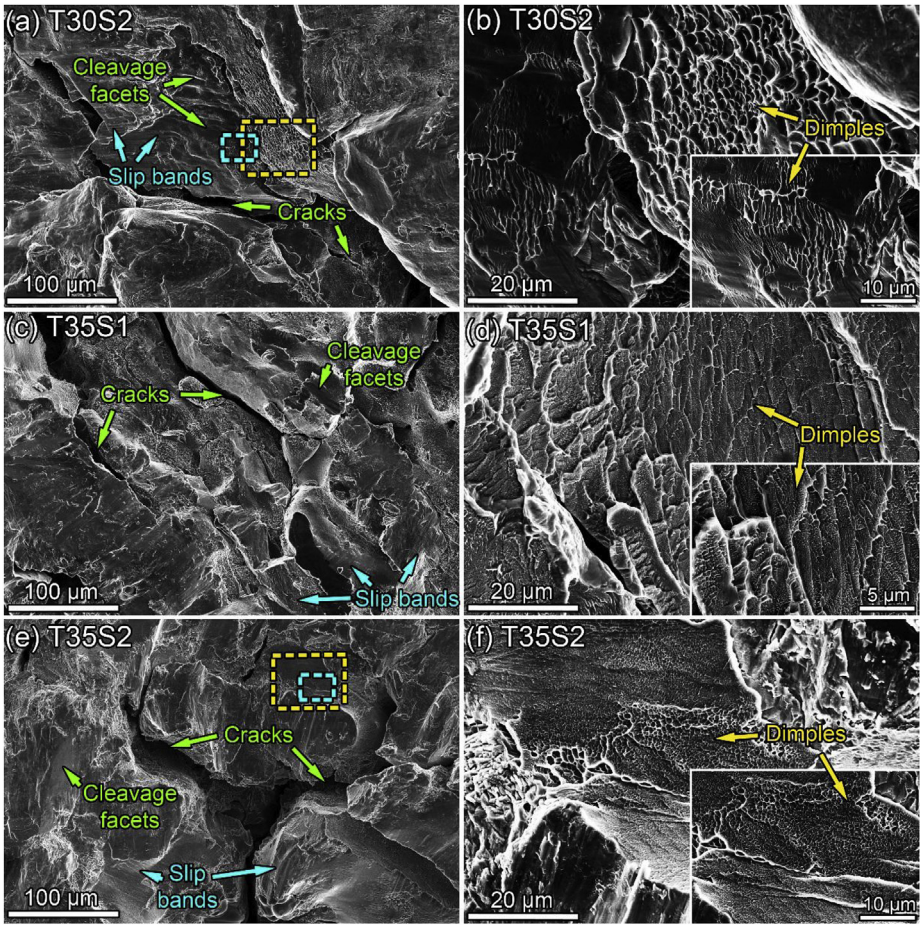

Fig. 8. The fractured morphologies of (a) T30S2, (c) T35S1 and (e) T35S2. (b) and (f) are the high-magnification images of the regions shown using yellow-dashed rectangles in (a) and (e) respectively. (d) is the high-magnification image of the region close to the region shown in (c) and the inset image in (d) is the high-magnification image of the region in (d). The inset images in (b) and (f) are the high-magnification images of the regions shown using skyblue-dashed rectangles in (a) and (e) respectively. Note that the abbreviation pattern in the forms of TxSy is used to present names of the investigated alloys. (For interpretation of the references to colour in this figure legend, the reader is referred to the Web version of this article.)

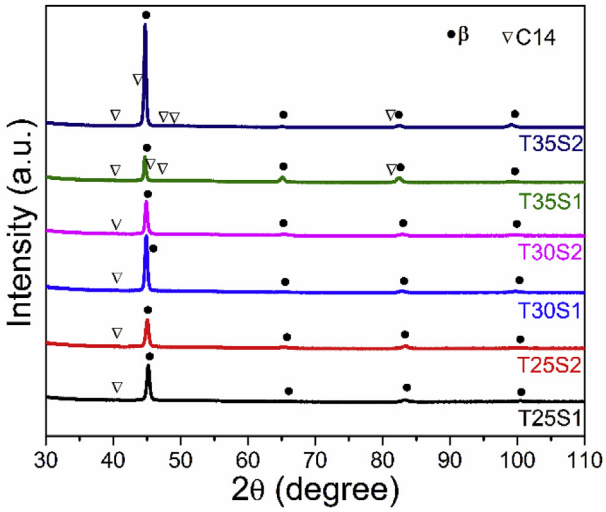

Fig. 9. The XRD profiles of the Ti-xZr-7Fe-ySn alloys after compression testing. Note that the abbreviation pattern in the forms of TxSy is used to present names of all the investigated alloys.

few small-sized (rod-like) morphologies of C14-Laves phase in T25S2 are also seen in Fig. 6b, which were not observed in the microstructure image of T25S2 (shown in Fig. 2). The presence of C14-Laves phase morphologies in T25S2 (Fig. 6b) is also an evidence of deformation induced phase transformation of C14-Laves phase in T25S2. The deformation induced Laves phase transformation (with a little amount) has also been reported in Refs. [70,71]. Moreover, a greater peak broadening is observed in the XRD profiles presented in Fig. 9 as compared to the XRD profiles presented in Fig. 1 for the Ti-xZr-7Fe-ySn alloys. The broadening of the peaks after compression testing occurs due to the distortion of lattice and the grain refinement.

Table 3 also presents the values of dislocation density and a product of σ_{max} and ϵ_f (PUSCS) for the Ti-xZr-7Fe-ySn alloys. The information on the dislocation-pinning can also be obtained based on the dislocation density and eventually, the strengthening behavior of the Ti-xZr-7Fe-ySn alloys can be analyzed. The lowest value of dislocation density is found in T25S1 ($0.21 \times 10^{15}\,m^{-2}$), whereas the highest value of dislocation density is found in T35S2 ($3.96 \times 10^{15}\,m^{-2}$) as T35S2 comprises the highest value of $V_{f,\ C14}$ amongst the investigated Ti-xZr-7Fe-ySn alloys. The values of dislocation density also suggest that the dislocation-pinning should have occurred at a minimum level in T25S1 and the dislocation-pinning should have occurred at a maximum level in T35S2. Although T25S1 comprises the Laves phase morphologies in the microstructure (Fig. 2), dislocation density of T25S2 is greater than T25S1. This indicates that the bright-faded morphologies in T25S2 also contribute in pinning the dislocations.

PUSCS is a quite popular parameter to evaluate the trade-off between strength and plasticity of a material [35,36]. In this work, as σ_{max} and ϵ_f are directly related to each other, PUSCS follows the same trend as σ_{max} and ϵ_f. Hence, T25S1 demonstrates the highest value of PUSCS (77.4 GPa %) and T35S2 demonstrates the lowest value of PUSCS (27.9 GPa %) in the present work (Table 3). Therefore, it can be inferred based on the results discussed that the precipitation strengthening features of T35S2 in terms of $\sigma_{0.2}$ (1359 ± 28 MPa), H (437 ± 23 HV) and dislocation density ($3.96 \times 10^{15}\,m^{-2}$) are better than the rest of the investigated alloys. By contrast, the deformation features including ϵ_f and ϵ_p of T25S1 are better than the rest of the investigated alloys.

4.2. Fracture analyses

In T30S1, T30S2, T35S1 and T35S2, other than primary cracks, voids are found inside the eutectic morphologies of Laves phase, which can be evidently seen in Fig. 6c inset (a series of yellow arrows). These voids form prior to the crack propagation. Furthermore, a series of parallel micro-cracks in the eutectic Laves phase can be seen in Fig. 6c inset for T30S1, which are indicated by a series of sky-blue arrows. These parallel micro-cracks in the Laves phase morphologies form due to slip activities occurring (on a same slip plane) in the nearer β grains. Therefore, these micro-cracks form parallel to each other inside the Laves phase morphologies. The similar kind of parallel micro-cracks are also found in the eutectic Laves phase morphologies of T30S2, T35S1 and T35S2 (the inset images of Fig. 6d–f). In general, slip bands form easily in a phase comprising a bcc structure as compared to a phase comprising an hcp structure because a bcc structure comprises a greater number of slip systems than an hcp structure [63,72,73]. Therefore, Peierls stress or lattice friction stress (the minimum shear stress required to move a dislocation over a specific matrix/phase) remains low for a phase with a bcc structure than that for a phase with an hcp structure [74]. As a result, in the present work, dislocations can easily move in the β (bcc) matrix than in a C14 (hcp) phase. Furthermore, slip bands in a particular grain form in different slip planes depending on the number of active slip systems in that grain [74]. However, it is difficult for slip bands to pass over the grain boundaries and/or second phase particles (with different crystal structure) because grain boundaries comprise detects in atomic sequence and second phase comprise the different lattice configuration [63]. Therefore, in the present work, slip bands form only in the β grains and dislocation pile up should have occurred at the phase boundaries of Laves-C14 phase because slip transfer from β (bcc) phase to Laves-C14 (hcp) phase remains difficult. Eventually, the morphologies of Laves-C14 phase fail due to not sustaining dislocation-pinning stress produced by dislocations/slip bands [73]. Consequently, parallel micro-cracks form in the eutectic Laves phase morphologies of T30S1, T30S2, T35S1 and T35S2. This also infers (based on the results discussed above) that among the β, bright-faded and Laves phase morphologies shown in this work, the Peierls stress should be the lowest in the β matrix, followed by the bright-faded morphologies and the highest in the Laves phase morphologies. Therefore, the bright-faded morphologies should be harder than the β matrix but softer than the Laves phase morphologies. Finally, it can be deduced that the results of the mechanical and fracture characterizations are in good agreement with the features of the microstructure analyzed in the present work.

5. Conclusions

The quantities of Zr and Sn have been varied to tailor the mechanical properties using a C14 type Laves phase in the Ti-xZr-7Fe-ySn (x = 25, 30, 35 wt% and y = 1, 2 wt%) alloys. The effects of compositional quantities (i.e., Zr and Sn) on the microstructure, mechanical and fracture properties for the Ti-xZr-7Fe-ySn alloys have been examined in this work and following concluding remarks have been made.

- Phase and microstructure analyses detect a C14 type Laves phase with a hexagonal close-packed structure and a dominant β phase with a body-centered cubic structure in the as-cast condition of all the investigated alloys except Ti-25Zr-7Fe-2Sn which shows a single β phase.
- The compositional effects in terms of the quantities of Zr and Sn greatly influence the volume fraction of the Laves phase. Furthermore, as the volume fraction of the Laves phase increases the values of other microstructural features such as lamellar spacing inside the eutectic-Laves phase morphologies, length and width of Laves phase morphologies increase.
- As the quantities of Zr and Sn increase, yield strength, hardness and dislocation density also increase, whereas ultimate strength, compressive strain at failure and plastic strain decrease in the present work.
- Among all the Ti-xZr-7Fe-ySn alloys analyzed in the present work, Ti-25Zr-7Fe-1Sn demonstrates the highest values of compressive strain at failure (36.2%), plastic strain (31.9%) and ultimate strength (2140 MPa), whereas Ti-35Zr-7Fe-2Sn exhibits the highest value of yield strength (1359 MPa), hardness (437 HV) and dislocation density ($3.96 \times 10^{15}\ m^{-2}$). Ti-25Zr-7Fe-1Sn shows the best trade-off in terms of the product of ultimate strength and plasticity (77.4 GPa %) in this work.
- Ti-25Zr-7Fe-1Sn is suitable for engineering applications where alloys are selected considering ultimate strength and compressive strain at failure; whereas Ti-35Zr-7Fe-2Sn is suitable for engineering applications where alloys are selected considering yield strength and hardness.
- The results of the microstructure, mechanical and fracture properties analyzed in this work by varying the quantities of Zr and Sn in Ti alloys are useful to develop an improved Laves phase alloy.

Acknowledgement

The authors would like to acknowledge the financial supports provided by National Natural Science Foundation of China under a grant no. 51674167 and Open foundation of Guangxi Key Laboratory of Processing for Non-ferrous Metals and Featured Materials, Guangxi University under a grant no. 2019GXYSOF01.

References

[1] F. Stein, M. Palm, G. Sauthoff, Structure and stability of Laves phases. Part I. Critical assessment of factors controlling Laves phase stability, Intermetallics 12 (2004) 713–720 https://doi.org/10.1016/j.intermet.2004.02.010.
[2] F. Chu, D.J. Thoma, P.G. Kotula, S. Gerstl, T.E. Mitchell, I.M. Anderson, J. Bentley, Phase stability and defect structure of the C15 Laves phase $Nb(Cr,V)_2$, Acta Mater. 46 (1998) 1759–1769 https://doi.org/10.1016/S1359-6454(97)00291-7.
[3] S. Huang, X. Zhang, Y. Jiang, Y. Jiang, C. Mao, D. Wu, L. Zhang, L. Liu, Experimental investigation of Ti-Nb-Co ternary system at 1000°C, Mater. Des. 115 (2017) 170–178 https://doi.org/10.1016/j.matdes.2016.11.056.
[4] J. Nei, K. Young, S.O. Salley, K.Y.S. Ng, Determination of C14/C15 phase abundance in Laves phase alloys, Mater. Chem. Phys. 136 (2012) 520–527 https://doi.org/10.1016/j.matchemphys.2012.07.020.
[5] S. Scudino, P. Donnadieu, K.B. Surreddi, K. Nikolowski, M. Stoica, J. Eckert, Microstructure and mechanical properties of Laves phase-reinforced Fe-Zr-Cr alloys, Intermetallics 17 (2009) 532–539 https://doi.org/10.1016/j.intermet.2009.01.007.
[6] A.I. Taub, R.L. Fleischer, Intermetallic compounds for high-temperature structural use, Science 243 (1989) 616–621 https://doi.org/10.1126/science.243.4891.616.
[7] C. Zehnder, K. Czerwinski, K.D. Molodov, S. Sandlöbes-Haut, J.S.K.L. Gibson, S. Korte-Kerzel, Plastic deformation of single crystalline C14 Mg_2Ca Laves phase at room temperature, Mater. Sci. Eng. A 759 (2019) 754–761 https://doi.org/10.1016/j.msea.2019.05.092.
[8] M. Zubair, S. Sandlöbes, M.A. Wollenweber, C.F. Kusche, W. Hildebrandt, C. Broeckmann, S. Korte-Kerzel, On the role of Laves phases on the mechanical properties of Mg-Al-Ca alloys, Mater. Sci. Eng. A 756 (2019) 272–283 https://doi.org/10.1016/j.msea.2019.04.048.
[9] C.D. Rabadia, Y.J. Liu, L. Wang, H. Sun, L.C. Zhang, Laves phase precipitation in Ti-Zr-Fe-Cr alloys with high strength and large plasticity, Mater. Des. 154 (2018) 228–238 https://doi.org/10.1016/j.matdes.2018.05.035.
[10] C.D. Rabadia, Y.J. Liu, S.F. Jawed, L. Wang, Y.H. Li, X.H. Zhang, T.B. Sercombe, H. Sun, L.C. Zhang, Improved deformation behavior in Ti-Zr-Fe-Mn alloys comprising the C14 type Laves and β phases, Mater. Des. 160 (2018) 1059–1070 https://doi.org/10.1016/j.matdes.2018.10.049.
[11] Y. Liu, S. Li, H. Wang, W. Hou, Y. Hao, R. Yang, T. Sercombe, L.C. Zhang, Microstructure, defects and mechanical behavior of beta-type titanium porous structures manufactured by electron beam melting and selective laser melting, Acta Mater. 113 (2016) 56–67 https://doi.org/10.1016/j.actamat.2016.04.029.
[12] Y.J. Liu, H.L. Wang, S.J. Li, S.G. Wang, W.J. Wang, W.T. Hou, Y.L. Hao, R. Yang, L.C. Zhang, Compressive and fatigue behavior of beta-type titanium porous structures fabricated by electron beam melting, Acta Mater. 126 (2017) 58–66 https://doi.org/10.1016/j.actamat.2016.12.052.
[13] L.C. Zhang, D. Klemm, J. Eckert, Y.L. Hao, T.B. Sercombe, Manufacture by selective laser melting and mechanical behavior of a biomedical Ti–24Nb–4Zr–8Sn alloy, Scr. Mater. 65 (2011) 21–24 https://doi.org/10.1016/j.scriptamat.2011.03.024.
[14] P. Qin, Y. Chen, Y.-J. Liu, J. Zhang, L.-Y. Chen, Y. Li, X. Zhang, C. Cao, H. Sun, L.-C. Zhang, Resemblance in corrosion behavior of selective laser melted and

traditional monolithic β Ti-24Nb-4Zr-8Sn alloy, ACS Biomater. Sci. Eng. 5 (2019) 1141–1149 https://doi.org/10.1021/acsbiomaterials.8b01341.
[15] P. Qin, Y. Liu, T.B. Sercombe, Y. Li, C. Zhang, C. Cao, H. Sun, L.C. Zhang, Improved corrosion resistance on selective laser melting produced Ti-5Cu alloy after heat treatment, ACS Biomater. Sci. Eng. 4 (2018) 2633–2642 https://doi.org/10.1021/acsbiomaterials.8b00319.
[16] N. Hafeez, S. Liu, E. Lu, L. Wang, R. Liu, W. lu, L.-C. Zhang, Mechanical behavior and phase transformation of β-type Ti-35Nb-2Ta-3Zr alloy fabricated by 3D-Printing, J. Alloy. Comp. 790 (2019) 117–126 https://doi.org/10.1016/j.jallcom.2019.03.138.
[17] C.D. Rabadia, Y.J. Liu, G.H. Cao, Y.H. Li, C.W. Zhang, T.B. Sercombe, H. Sun, L.C. Zhang, High-strength β stabilized Ti-Nb-Fe-Cr alloys with large plasticity, Mater. Sci. Eng. A 732 (2018) 368–377 https://doi.org/10.1016/j.msea.2018.07.031.
[18] L.C. Zhang, L.Y. Chen, A review on biomedical titanium alloys: recent progress and prospect, Adv. Eng. Mater. 21 (2019) 1801215 https://doi.org/10.1002/adem.201801215.
[19] J. Wang, Z. Qin, F. Xiong, S. Wang, X. Lu, C. Li, Design and preparation of low-cost α + β titanium alloy based on assessment of Ti-Al-Fe-Cr system, Mater. Sci. Eng. A 732 (2018) 63–69 https://doi.org/10.1016/j.msea.2018.06.101.
[20] L. Zhang, H.-B. Lu, C. Mickel, J. Eckert, Ductile ultrafine-grained Ti-based alloys with high yield strength, Appl. Phys. Lett. 91 (2007) 051906https://doi.org/10.1063/1.2766861.
[21] X.H. Min, S. Emura, N. Sekido, T. Nishimura, K. Tsuchiya, K. Tsuzaki, Effects of Fe addition on tensile deformation mode and crevice corrosion resistance in Ti–15Mo alloy, Mater. Sci. Eng. A 527 (2010) 2693–2701 https://doi.org/10.1016/j.msea.2009.12.050.
[22] Y.D. Shi, L.N. Wang, S.X. Liang, Q. Zhou, B. Zheng, A high Zr-containing Ti-based alloy with ultralow Young's modulus and ultrahigh strength and elastic admissible strain, Mater. Sci. Eng. A 674 (2016) 696–700 https://doi.org/10.1016/j.msea.2016.08.038.
[23] L. Chen, J. Li, Y. Zhang, L.-C. Zhang, W. Lu, L. Zhang, L. Wang, D. Zhang, Effects of alloyed Si on the autoclave corrosion performance and periodic corrosion kinetics in Zr–Sn–Nb–Fe–O alloys, Corros. Sci. 100 (2015) 651–662 https://doi.org/10.1016/j.corsci.2015.08.043.
[24] L. Chen, J. Li, Y. Zhang, L.-C. Zhang, W. Lu, L. Wang, L. Zhang, D. Zhang, Zr–Sn–Nb–Fe–Si–O alloy for fuel cladding candidate: Processing, microstructure, corrosion resistance and tensile behavior, Corros. Sci. 100 (2015) 332–340 https://doi.org/10.1016/j.corsci.2015.08.005.
[25] Y.J. Liu, X.P. Li, L.C. Zhang, T.B. Sercombe, Processing and properties of topologically optimised biomedical Ti–24Nb–4Zr–8Sn scaffolds manufactured by selective laser melting, Mater. Sci. Eng. A 642 (2015) 268–278 https://doi.org/10.1016/j.msea.2015.06.088.
[26] S.F. Jawed, C.D. Rabadia, Y.J. Liu, L.Q. Wang, Y.H. Li, X.H. Zhang, L.C. Zhang, Mechanical characterization and deformation behavior of β-stabilized Ti-Nb-Sn-Cr alloys, J. Alloy. Comp. 792 (2019) 684–693 https://doi.org/10.1016/j.jallcom.2019.04.079.
[27] Y.J. Liu, Y.S. Zhang, L.C. Zhang, Transformation-induced plasticity and high strength in beta titanium alloy manufactured by selective laser melting, Materialia 6 (2019) 100299 https://doi.org/10.1016/j.mtla.2019.100299.
[28] J.M. Park, K.B. Kim, W.T. Kim, M.H. Lee, J. Eckert, D.H. Kim, High strength ultrafine eutectic Fe-Nb-Al composites with enhanced plasticity, Intermetallics 16 (2008) 642–650 https://doi.org/10.1016/j.intermet.2008.01.005.
[29] J.C. Wang, Y.J. Liu, P. Qin, S.X. Liang, T.B. Sercombe, L.C. Zhang, Selective laser melting of Ti–35Nb composite from elemental powder mixture: microstructure, mechanical behavior and corrosion behavior, Mater. Sci. Eng. A 760 (2019) 214–224 https://doi.org/10.1016/j.msea.2019.06.001.
[30] C.L. Yang, Z.J. Zhang, P. Zhang, C.Y. Cui, Z.F. Zhang, Synchronous improvement of the strength and plasticity of Ni-Co based superalloys, Mater. Sci. Eng. A 736 (2018) 100–104 https://doi.org/10.1016/j.msea.2018.08.012.
[31] V. Raghavan, Fe-Ti-Zr (Iron-Titanium-Zirconium), J. Phase Equilibria 31 (2010) 469 https://doi.org/10.1007/s11669-010-9751-3.
[32] L. Zeng, G. Xu, L. Liu, W. Bai, L. Zhang, Experimental investigation of phase equilibria in the Ti-Fe-Zr system, Calphad 61 (2018) 20–32 https://doi.org/10.1016/j.calphad.2018.02.005.
[33] S.F. Aricó, L.M. Gribaudo, The Sn–Ti–Zr system: equilibrium phases at 900°C, J. Nucl. Mater. 288 (2001) 217–221 https://doi.org/10.1016/S0022-3115(00)00707-8.
[34] V.A. Saltykov, K.A. Meleshevich, A.V. Samelyuk, O.M. Verbytska, M.V. Bulanova, Isothermal section at 1400°C of the Ti–Zr–Sn system, J. Alloy. Comp. 459 (2008) 348–353 https://doi.org/10.1016/j.jallcom.2007.04.268.
[35] X. Li, R. Song, N. Zhou, J. Li, An ultrahigh strength and enhanced ductility cold-rolled medium-Mn steel treated by intercritical annealing, Scr. Mater. 154 (2018) 30–33 https://doi.org/10.1016/j.scriptamat.2018.05.016.
[36] S. Liu, Z. Xiong, H. Guo, C. Shang, R.D.K. Misra, The significance of multi-step partitioning: Processing-structure-property relationship in governing high strength-high ductility combination in medium-manganese steels, Acta Mater. 124 (2017) 159–172 https://doi.org/10.1016/j.actamat.2016.10.067.
[37] G.K. Williamson, R.E. Smallman III., Dislocation densities in some annealed and cold-worked metals from measurements on the X-ray debye-scherrer spectrum, Philos. Mag.: A Journal of Theoretical Experimental and Applied Physics 1 (1956) 34–46 https://doi.org/10.1080/14786435608238074.
[38] A. Shabani, M.R. Toroghinejad, A. Shafyei, P. Cavaliere, Effect of cold-rolling on microstructure, texture and mechanical properties of an equiatomic FeCrCuMnNi high entropy alloy, Materialia 1 (2018) 175–184 https://doi.org/10.1016/j.mtla.2018.06.004.
[39] A.P. Zhilyaev, A.A. Samigullina, A.A. Nazarov, E.R. Shayakhmetova, Structure evolution in coarse-grained nickel under ultrasonic treatment, Mater. Sci. Eng. A 731 (2018) 231–238 https://doi.org/10.1016/j.msea.2018.06.052.
[40] W.D. Callister, Fundamentals of Materials Science and Engineering, John Wiley & Sons. Inc., New York, 2000.
[41] B.D. Cullity, S.R. Stock, Elements of X-Ray Diffraction, third ed., Prentice-Hall, New York, 2001.
[42] C. Yang, L.H. Liu, Q.R. Cheng, D.D. You, Y.Y. Li, Equiaxed grained structure: a structure in titanium alloys with higher compressive mechanical properties, Mater. Sci. Eng. A 580 (2013) 397–405 https://doi.org/10.1016/j.msea.2013.05.066.
[43] K. Bazzi, A. Rathi, V.M. Meka, R. Goswami, T.V. Jayaraman, Significant reduction in intrinsic coercivity of high-entropy alloy FeCoNiAl0.375Si0.375 comprised of supersaturated f.c.c. phase, Materialia 6 (2019) 100293 https://doi.org/10.1016/j.mtla.2019.100293.
[44] C. Suryanarayana, M.G. Norton, X-ray Diffraction: a Practical Approach, Springer Science & Business Media, Berlin, 2013.
[45] G.K. Williamson, W.H. Hall, X-ray line broadening from filed aluminium and wolfram, Acta Metall. 1 (1953) 22–31 https://doi.org/10.1016/0001-6160(53)90006-6.
[46] Y.J. Yin, J.Q. Sun, J. Guo, X.F. Kan, D.C. Yang, Mechanism of high yield strength and yield ratio of 316 L stainless steel by additive manufacturing, Mater. Sci. Eng. A 744 (2019) 773–777 https://doi.org/10.1016/j.msea.2018.12.092.
[47] F. Laliberte, M. Li, J. Almer, L. Liu, In-situ synchrotron X-ray study of microstructural evolution during creep deformation in Grade 91 steel, Mater. Sci. Eng. A 737 (2018) 115–123 https://doi.org/10.1016/j.msea.2018.09.033.
[48] L.C. Zhang, Y. Liu, S. Li, Y. Hao, Additive manufacturing of titanium alloys by electron beam melting: a review, Adv. Eng. Mater. 20 (2018) 1700842 https://doi.org/10.1002/adem.201700842.
[49] Y. Liu, S. Li, W. Hou, S. Wang, Y. Hao, R. Yang, T.B. Sercombe, L.-C. Zhang, Electron beam melted beta-type Ti–24Nb–4Zr–8Sn porous structures with high strength-to-modulus ratio, J. Mater. Sci. Technol. 32 (2016) 505–508 https://doi.org/10.1016/j.jmst.2016.03.020.
[50] G.A. Song, T.E. Kim, D.H. Kim, F. Prima, K.B. Kim, Influence of hetero-duplex structure on mechanical properties of Mg–Al/Cu–Zn alloys, Mater. Sci. Eng. A 528 (2010) 371–378 https://doi.org/10.1016/j.msea.2010.09.036.
[51] M.J. Bermingham, S.D. McDonald, M.S. Dargusch, Effect of trace lanthanum hexaboride and boron additions on microstructure, tensile properties and anisotropy of Ti-6Al-4V produced by additive manufacturing, Mater. Sci. Eng. A 719 (2018) 1–11 https://doi.org/10.1016/j.msea.2018.02.012.
[52] Z. Liu, Q. Gao, H. Zhang, S. Luo, X. Zhang, W. Li, Y. Jiang, H. Li, EBSD analysis and mechanical properties of alumina-forming austenitic steel during hot deformation and annealing, Mater. Sci. Eng. A 755 (2019) 106–115 https://doi.org/10.1016/j.msea.2019.04.005.
[53] L. Zhang, J. Das, H. Lu, C. Duhamel, M. Calin, J. Eckert, High strength Ti–Fe–Sn ultrafine composites with large plasticity, Scr. Mater. 57 (2007) 101–104 https://doi.org/10.1016/j.scriptamat.2007.03.031.
[54] B. Song, B. Sanborn, Relationship of compressive stress-strain response of engineering materials obtained at constant engineering and true strain rates, Int. J. Impact Eng. 119 (2018) 40–44 https://doi.org/10.1016/j.ijimpeng.2018.05.001.
[55] O.N. Senkov, S. Rao, K.J. Chaput, C. Woodward, Compositional effect on microstructure and properties of NbTiZr-based complex concentrated alloys, Acta Mater. 151 (2018) 201–215 https://doi.org/10.1016/j.actamat.2018.03.065.
[56] S.F. Jawed, C.D. Rabadia, Y.J. Liu, L. Wang, Y.H. Li, X.H. Zhang, L.C. Zhang, Beta-type Ti-Nb-Zr-Cr alloys with large plasticity and significant strain hardening, Mater. Des. 181 (2019) 108064 https://doi.org/10.1016/j.matdes.2019.108064.
[57] D.H. Krinsley, K. Pye, S. Boggs Jr., N.K. Tovey, Backscattered Scanning Electron Microscopy and Image Analysis of Sediments and Sedimentary Rocks, Cambridge University Press, Cambridge, 2005.
[58] L.C. Zhang, Z.Q. Shen, J. Xu, Glass formation in a (Ti, Zr, Hf)–(Cu, Ni, Ag)–Al high-order alloy system by mechanical alloying, J. Mater. Res. 18 (2003) 2141–2149 https://doi.org/10.1557/JMR.2003.0300.
[59] J. Chakrabarty, Applied Plasticity, Springer, New York, 2000.
[60] C. Yang, O. Muránsky, H. Zhu, G.J. Thorogood, H. Huang, X. Zhou, On the origin of strengthening mechanisms in Ni-Mo alloys prepared via powder metallurgy, Mater. Des. 113 (2017) 223–231 https://doi.org/10.1016/j.matdes.2016.10.024.
[61] B.A. Sun, W.H. Wang, The fracture of bulk metallic glasses, Prog. Mater. Sci. 74 (2015) 211–307 https://doi.org/10.1016/j.pmatsci.2015.05.002.
[62] Y.H. Li, C. Yang, F. Wang, H.D. Zhao, S.G. Qu, X.Q. Li, W.W. Zhang, Y.Y. Li, Biomedical TiNbZrTaSi alloys designed by d-electron alloy design theory, Mater. Des. 85 (2015) 7–13 https://doi.org/10.1016/j.matdes.2015.06.176.
[63] D. Hull, D.J. Bacon, Introduction to Dislocations, fifth ed., Butterworth-Heinemann, Oxford, 2011.
[64] H. Zhan, W. Zeng, G. Wang, D. Kent, M. Dargusch, On the deformation mechanisms and strain rate sensitivity of a metastable β Ti–Nb alloy, Scr. Mater. 107 (2015) 34–37 https://doi.org/10.1016/j.scriptamat.2015.05.014.
[65] D. Udler, D.N. Seidman, Solute-atom interactions with low-angle twist boundaries, Scr. Metall. Mater. 26 (1992) 449–454 https://doi.org/10.1016/0956-716X(92)90628-R.
[66] F. Stein, G. Sauthoff, M. Palm, Experimental determination of intermetallic phases, phase equilibria, and invariant reaction temperatures in the Fe-Zr system, J. Phase Equilibria 23 (2002) 480 https://doi.org/10.1361/105497102770331172.
[67] M.I. Isik, A. Kostka, V.A. Yardley, K.G. Pradeep, M.J. Duarte, P.P. Choi, D. Raabe, G. Eggeler, The nucleation of Mo-rich Laves phase particles adjacent to M23C6 micrograin boundary carbides in 12% Cr tempered martensite ferritic steels, Acta Mater. 90 (2015) 94–104 https://doi.org/10.1016/j.actamat.2015.01.027.
[68] X. Li, J.J. Shi, C.H. Wang, G.H. Cao, A.M. Russell, Z.J. Zhou, C.P. Li, G.F. Chen,

Effect of heat treatment on microstructure evolution of Inconel 718 alloy fabricated by selective laser melting, J. Alloy. Comp. 764 (2018) 639–649 https://doi.org/10.1016/j.jallcom.2018.06.112.
[69] L. Wang, W. Lu, J. Qin, F. Zhang, D. Zhang, Influence of cold deformation on martensite transformation and mechanical properties of Ti–Nb–Ta–Zr alloy, J. Alloy. Comp. 469 (2009) 512–518 https://doi.org/10.1016/j.jallcom.2008.02.032.
[70] L.M. Kang, C. Yang, F. Wang, S.G. Qu, X.Q. Li, W.W. Zhang, Deformation induced precipitation of $MgZn_2$-type laves phase in Ti-Fe-Co alloy, J. Alloy. Comp. 778 (2019) 795–802 https://doi.org/10.1016/j.jallcom.2018.11.236.
[71] D.V. Louzguine-Luzgin, L.V. Louzguina-Luzgina, V.I. Polkin, A. Inoue, Deformation-induced transformations in $Ti_{60}Fe_{20}Co_{20}$ alloy, Scr. Mater. 57 (2007) 445–448 https://doi.org/10.1016/j.scriptamat.2007.04.021.
[72] C. Yang, L.M. Kang, X.X. Li, W.W. Zhang, D.T. Zhang, Z.Q. Fu, Y.Y. Li, L.C. Zhang, E.J. Lavernia, Bimodal titanium alloys with ultrafine lamellar eutectic structure fabricated by semi-solid sintering, Acta Mater. 132 (2017) 491–502 https://doi.org/10.1016/j.actamat.2017.04.062.
[73] C.D. Rabadia, Y.J. Liu, L.Y. Chen, S.F. Jawed, L.Q. Wang, H. Sun, L.C. Zhang, Deformation and strength characteristics of Laves phases in titanium alloys, Mater. Des. 179 (2019) 107891 https://doi.org/10.1016/j.matdes.2019.107891.
[74] R.W. Hertzberg, R.P. Vinci, J.L. Hertzberg, Deformation and Fracture Mechanics of Engineering Materials, fifth ed., Wiley, Hoboken, NJ, 2013.